SPECIAL TOPIC — A 40th Anniversary Celebration: Physics Research and Innovation at Ningbo University

Gain-free quantum sensing via $\mathcal{PT}$-like-induced coherence enhancement in cavity-magnomechanical system

Jin-Yu Mao(毛金玉), Zi-Hao Ma(马梓浩), Feng Zhang(张凤), Jiong Cheng(程泂)[†], and Wen-Zhao Zhang(张闻钊)[‡]

Institute of Fundamental Physics and Quantum Technology and Department of Physics, School of Physical Science and Technology, Ningbo University, Ningbo 315211, *China*

(Received 11 May 2026; revised manuscript received 21 June 2026; accepted manuscript online 24 June 2026)

A gain-free $\mathcal{PT}$-like-induced coherence enhancement quantum sensing scheme is implemented in a cavity-magnomechanical system. In the absence of a conventional gain–loss balance, $\mathcal{PT}$-like behavior arises near an exceptional point, where symmetry and its breaking lead to robust quantum coherence. The optimal sensing regime is directly determined by the phase of the coherent parameters. Governed alternately by the $\mathcal{PT}$-symmetric and symmetry-broken regimes, this quantum coherence can either suppress or enhance the signal-to-noise ratio, depending on the probe configuration. These results provide a clear and experimentally friendly framework for optimizing quantum-coherence-based sensing in realistic hybrid quantum systems.

Keywords: $\mathcal{PT}$-symmetric, cavity-magnomechanical system, quantum sensing

PACS: 03.65.Ta, 42.50.–p, 42.50.Wk

DOI: 10.1088/1674-1056/ae8163 **CSTR:** 32038.14.CPB.ae8163

1. Introduction

Quantum precision measurement seeks to exploit unique quantum resources, such as entanglement, squeezing, and coherence, to surpass classical limits.[1] In recent years, non-Hermitian physics, with parity-time ($\mathcal{PT}$) symmetry as a prominent example,[2–4] has opened new approaches in this field. By balancing gain and loss, $\mathcal{PT}$-symmetric systems can host non-Hermitian degeneracies known as exceptional points (EPs), where both eigenvalues and eigenvectors coalesce.[5–7] Near EPs, the eigenvalue spectrum exhibits an enhanced response to external perturbations, providing a promising mechanism for ultra-sensitive parameter estimation. Notable examples include sensing schemes based on high-order EPs[3] and $\mathcal{PT}$-symmetry-enhanced cavity optomechanical magnetometry.[8] Nevertheless, precision measurement protocols based on conventional $\mathcal{PT}$-symmetry face significant challenges. The implementation of controlled, low-noise gain remains experimentally demanding in most quantum platforms, such as cold atoms,[9,10] spin systems,[11] and microwave photonics circuits,[12,13] thus limiting practical realizations. Moreover, the operation of EP-based sensors relies critically on the precise balance between gain and loss.[14] This balance is inherently fragile, with small parameter fluctuations shifting the system away from the EP and significantly degrading sensitivity, thereby hindering stable device operation.

To overcome these limitations, anti-$\mathcal{PT}$-symmetric systems have been proposed. As a natural extension of $\mathcal{PT}$-symmetry,[15,16] anti-$\mathcal{PT}$-symmetric systems are governed by dissipation and coupling. In contrast to $\mathcal{PT}$-symmetric systems, which can exhibit real eigenvalues, anti-$\mathcal{PT}$-symmetric systems possess purely imaginary eigenvalues.[17] In this regime, the resonance frequency remains invariant under parameter perturbations. This behavior is known as frequency pinning.[18] Only the decay rate, corresponding to the imaginary part of the eigenvalue, is perturbed. This property suggests that anti-$\mathcal{PT}$-symmetry can realize comparable sensing enhancements without the need for active gain.[19–22] For instance, it enables enhanced detection of weak anharmonicities via coherence effects in dissipatively coupled anti-$\mathcal{PT}$-symmetric systems, as well as efficient protocols for identifying weak nonlinearities.[23] Moreover, dissipative coupling in such platforms can generate quantum correlations,[24] and anti-$\mathcal{PT}$-symmetry has also been shown to facilitate microwave negative refractive index in coupled photon-magnon hybrid systems.[25] Despite these advantages, experimental realizations of anti-$\mathcal{PT}$-symmetry remain limited to bulky platforms or systems that rely on optical gain.[17] These considerations motivate a reexamination of the physical mechanisms underlying EP-enhanced sensing. One widely discussed mechanism is the amplification associated with non-Hermitian singularities, which arises from the EP's extreme parameter sensitivity[26] and consequently amplifies both signal and noise.[27] This inevitably degrades detection perfor-

[†]Corresponding author. E-mail: chengjiong@nbu.edu.cn

[‡]Corresponding author. E-mail: zhangwenzhao@nbu.edu.cn

© 2026 Chinese Physical Society and IOP Publishing Ltd. All rights, including for text and data mining, AI training, and similar technologies, are reserved.

CPB Online In-Press

mance. Another mechanism originates from coherent quantum effects.[28] In the vicinity of the EP, near-degenerate supermodes give rise to strong quantum coherence, which suppresses non-coherent noise.[29] This coherence enables an intrinsic amplification mechanism that does not rely on gain.[30] In contrast, gain primarily compensates for dissipation and improves the signal-to-noise ratio, without contributing to coherence generation.

Motivated by these considerations, we propose an experimentally feasible $\mathcal{PT}$-like quantum metrology scheme that operates without active gain or complex coupling. Our approach eliminates the requirement for stringent gain-loss balance and active control over coupling and dissipation. Instead, it harnesses quantum coherence near degeneracies in generic quantum systems to achieve signal enhancement and improved sensitivity. We demonstrate this principle using a cavity-magnomechanical platform, which has recently attracted significant interest, to achieve enhanced detection of both mechanical and magnetic signals. The paper is organized as follows. In Section 2, we introduce the model, derive its solutions, and analyze the detection mechanism within the supermode framework. In Section 3, we evaluate the sensing performance of the system via mechanical and magnonic ports. Finally, Section 4 provides a summary and discussion.

2. Model and Hamiltonian

The cavity-magnomechanical system (CMM), which is able to couple with a variety of physical quantities such as light, sound, and magnetism, is a highly promising detection platform. As shown in Fig. 1(a), a CMM is considered with the Hamiltonian[31]

$$\frac{\hat{H}}{\hbar} = \frac{\omega_b}{2}(\hat{q}^2+\hat{p}^2)+\sum_{j=c,m}(\omega_j+g_j\hat{q})\,\hat{j}^\dagger\hat{j} + \mathrm{i}\varepsilon_j(\hat{j}^\dagger \mathrm{e}^{-\mathrm{i}\omega_{d,j}t}-\hat{j}\,\mathrm{e}^{\mathrm{i}\omega_{d,j}t}), \tag{1}$$

where $\hat{c}$ ($\hat{c}^\dagger$) and $\hat{m}$ ($\hat{m}^\dagger$) are the annihilation (creation) operators of the photon and magnon modes, respectively, $\hat{q}=(\hat{b}+\hat{b}^\dagger)/\sqrt{2}$ and $\hat{p}=\mathrm{i}(\hat{b}^\dagger-\hat{b})\sqrt{2}$ are the dimensionless position and momentum of the vibration mode, and ω_j ($j=c,m,b$) are their resonance frequencies. $\omega_{d,j}$ is the driving frequency. Under strong-driving ($\varepsilon_j/\kappa_c \gg 1$) and weak-coupling ($g_j/\kappa_c \ll 1$) conditions, the linearized Hamiltonian is given by[32,33]

$$\frac{\hat{H}_L}{\hbar} = \omega_b\hat{b}^\dagger\hat{b}+\sum_{j=c,m}\Delta_j\hat{j}^\dagger\hat{j}+(G_j^*\hat{j}+G_j\hat{j}^\dagger)(\hat{b}+\hat{b}^\dagger), \tag{2}$$

where $\Delta_j=\omega_j-\omega_{d,j}+g_j\bar{q}$ is the driving-modified detuning, and $G_j=\bar{j}g_j/\sqrt{2}$ ($j=c,m$) is the driving-enhanced coupling rate for $\bar{j}\equiv\langle\hat{j}\rangle$ denoting the mean amplitude. In typical detection schemes, the optical mode serves as the output channel, while the magnon and mechanical modes act as sensing modes that couple to the signal. As shown in Fig. 1(a), the cavity mode c serves as the output channel. The signal of interest can be injected either via the magnon mode m (with mode b as an auxiliary) or via mode b (with mode m as an auxiliary), and is subsequently extracted from mode c. In the simplified cascaded schematic shown in the upper part of Fig. 1(b), signal transmission is predominantly governed by the effective coupling and dissipation between modes b and c, which are renormalized by the auxiliary mode although the latter is not directly observable.[34–37] The supermode framework, illustrated in the lower part of Fig. 1(b), provides a clearer perspective on the physical process. In this regime, as mode m (or b) is renormalized, the signal decomposes into two components that couple to the supermodes $\hat{b}_+$ and $\hat{b}_-$, respectively. Both components are simultaneously emitted through mode c, where their coherent interference arises, thereby enhancing the detection sensitivity. Under the resonance condition $\Delta_m \approx \omega_b$, the rotating-wave approximation is applied to the coupling between modes m and b. Incorporating the dissipation rates κ_c, κ_m, and γ of the photon, magnon, and phonon modes, respectively, the coefficient matrix governing the system's dynamical equations yields the following complex eigenvalues[6,38]

$$E_\pm = \omega_b-\frac{\mathrm{i}}{4}(\kappa_m+\gamma)\pm\sqrt{|G_m|^2-\frac{1}{16}(\kappa_m-\gamma)^2}. \tag{3}$$

The corresponding frequencies are $\omega_\pm=\mathrm{Re}(E_\pm)$ and the dissipations are $\kappa_\pm=2\mathrm{Im}(E_\pm)$. As shown in Fig. 2, we demonstrate how the frequency and dissipation of the supermode depend on the coupling strength. When the coupling strength satisfies $|G_m|=(\kappa_m-\gamma)/4\equiv G_p$, a phenomenon analogous to the EP appears.[39] The dissipation remains finite, as no standard gain-loss balance is present. Nevertheless, both the eigenfrequency and the dissipation become degenerate at this point. The $\mathcal{PT}$-symmetric and symmetry-broken regions are also separated by the EP,[40] exhibiting effects similar to those of a gain-included non-Hermitian system. The supermodes are obtained from the corresponding eigenstates of the system's coefficient matrix

$$\hat{b}_\pm = \alpha_\pm\hat{m}+\beta_\pm\,\mathrm{e}^{\mathrm{i}\theta_\pm}\hat{b}, \tag{4}$$

where the real superposition coefficient satisfies $|\alpha_\pm|^2+|\beta_\pm|^2=1$ and $\theta_\pm$ denotes the parameter-dependent local phase. It is worth noting that $\theta_\pm$ is a nontrivial function jointly determined by the system parameters G_m, κ_m, and γ, rather than being directly determined by the phase of G_m. Therefore, without loss of generality and for simplicity, we take all G_j to be real throughout the following discussion. This choice does not affect the essential physics, since $\theta_\pm$ remains fully tunable through the parameters $|G_m|$, κ_m, and γ. In the supermode ba-

CPB Online In-Press

sis, we rewrite the Hamiltonian as

$$\frac{\hat{H}_s}{\hbar} = \Delta_c \hat{c}^\dagger \hat{c} + \sum_{j=\pm}\left[\omega_j \hat{b}_j^\dagger \hat{b}_j + (G_c^* \hat{c} + G_c \hat{c}^\dagger)\left(\mu_j \hat{b}_j + \mu_j^* \hat{b}_j^\dagger\right)\right], \quad (5)$$

where $\mu_\pm = \frac{\alpha_\mp}{\alpha_\mp \beta_\pm e^{\theta_\pm} - \alpha_\pm \beta_\mp e^{\theta_\mp}}$. In our discussion, all systems are purely dissipative, with no gain introduced to balance the loss. As a result, the superposition coefficients take relatively complicated forms. We show the evolution of the corresponding superposition parameters in the supermode basis as functions of the coupling strength G_m in Fig. 3. As illustrated in Figs. 3(a) and 3(b), the superposition coefficients $\alpha_\pm$ and $\beta_\pm$ evolve continuously with increasing coupling strength G_m. In the weak-coupling region ($G_m \ll G_p$), the supermodes $\hat{b}_\pm$ remain close to the uncoupled (bare) modes, with each supermode dominated by either $\hat{b}$ or $\hat{m}$. As G_m increases, the coupling induces progressive hybridization between the two modes, leading to a redistribution of their weights. Near the critical point G_p, the system undergoes a $\mathcal{PT}$-symmetric transition, where the eigenmodes become strongly mixed. For $G_m \geq G_p$, the hybridization saturates, and both supermodes approach equal-weight superpositions with $|\alpha_\pm|^2 \approx |\beta_\pm|^2 \approx 1/2$, indicating fully hybridized normal modes.[41] A distinct transition is observed in the phase behavior shown in Fig. 3(c). For $G_m < G_p$, the system dynamics are primarily governed by amplitude hybridization, i.e., the relative weights of $\hat{b}$ and $\hat{m}$. In contrast, once the hybridization is saturated ($G_m \geq G_p$), the amplitude composition becomes essentially fixed, and the system enters a phase-dominated regime, where the local phase $\theta_\pm$ becomes the key parameter controlled by G_m. This marks a crossover from amplitude-controlled to phase-controlled dynamics, which is directly reflected in the effective coupling weights $\mu_\pm$ in the Hamiltonian $\hat{H}_s$, as shown in Figs. 3(d) and 3(e). Below G_p, $\mu_\pm$ are mainly characterized by amplitude variations associated with the hybridization process. Above G_p, however, their magnitudes become nearly equal, while their phases become separated, signaling a transition to phase modulation. The symmetry further clarifies this behavior, where the 0-symmetric structure modulates the real part (amplitude channel) and the $\pi/2$-symmetric structure modulates the imaginary part (phase channel).

By projecting the dynamical equations of the original Hamiltonian onto the supermode basis defined by the eigenstates in Eq. (4), we obtain

$$\dot{\hat{c}} = -(i\Delta_c + \frac{\kappa_c}{2})\hat{c} - iG_c \sum_{j=\pm}\left(\mu_j \hat{b}_j + \mu_j^* \hat{b}_j^\dagger\right) + \sqrt{\kappa_c}\hat{a}_{\rm in}, \quad (6a)$$

$$\dot{\hat{b}}_\pm = -(i\omega_\pm + \frac{\kappa_\pm}{2})\hat{b}_\pm - i\mu_\pm^*(G_c^* \hat{c} + G_c \hat{c}^\dagger) + \alpha_\pm \sqrt{\kappa_m}\hat{m}_{\rm in} + \beta_\pm e^{i\theta_\pm}\sqrt{\gamma}\hat{b}_{\rm in}. \quad (6b)$$

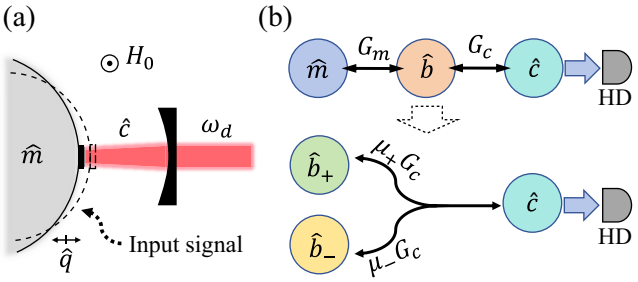


Fig. 1. (a) Hybrid cavity-magnomechanical system. The cavity mode c is the output channel. The signal is injected via the magnon mode m or the mechanical mode b (with one serving as the auxiliary mode), and extracted from c. (b) Upper part: simplified cascaded schematic, where signal transmission is governed by the effective coupling and dissipation between b and c. Lower part: supermode framework, where the signal decomposes into two components coupling to $\hat{b}_+$ and $\hat{b}_-$. HD: Homodyne detection.

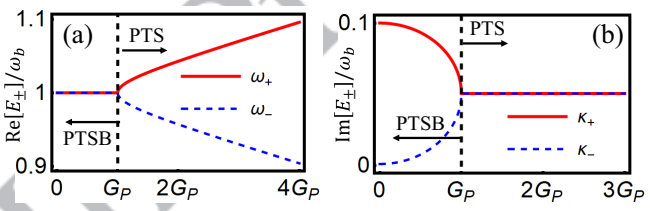


Fig. 2. The real (a) and imaginary (b) parts of the eigenenergy $E_\pm$. The parameters are $G_c = 0.1\omega_b$, $\kappa_m = \kappa_c = 0.1\omega_b$, $\gamma = 10^{-5}\omega_b$, $T_b = 10$ mK, and $\omega_b = 2\pi \times 10$ MHz. The labels PTS and PTSB denote the $\mathcal{PT}$-symmetric and symmetry-broken regions, respectively.

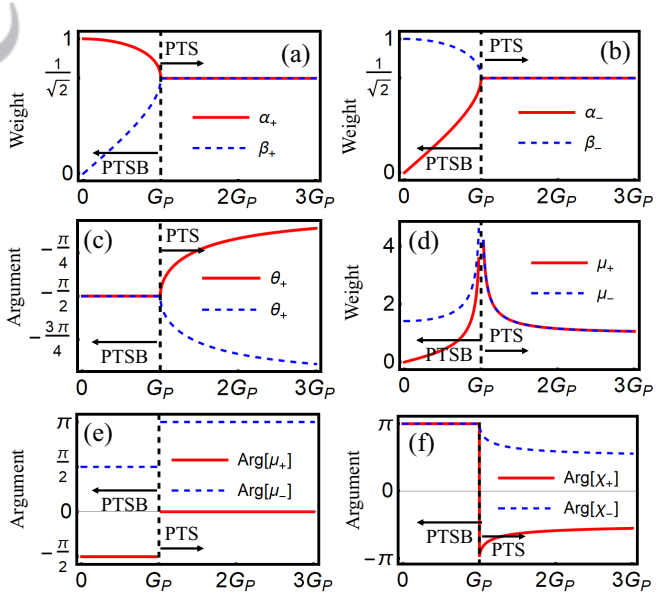


Fig. 3. (a) Superposition coefficients of the $\hat{b}_+$ mode as functions of G_m. (b) Superposition coefficients of the $\hat{b}_-$ mode as functions of G_m. (c) Local phases of the superposition for $\hat{b}_\pm$ as a function of G_m. (d) Magnitudes and (e) phases of the coupling weight $\mu_\pm$ in $\hat{H}_s$ as functions of G_m. (f) Phases of the susceptibilities of the supermodes $\hat{b}_\pm$. Other parameters are the same as in Fig. 2.

After Fourier transform, we have

$$\hat{c}(\omega) = \chi_c\left\{-iG_c \sum_{j=\pm}\left[\mu_j \hat{b}_j(\omega) + \mu_j^* \hat{b}_j^\dagger(-\omega)\right] + \sqrt{\kappa_c}\hat{a}_{\rm in}(\omega)\right\}, \quad (7a)$$

$$\hat{b}_\pm(\omega) = \chi_\pm\left\{-i\mu_\pm^*\left[G_c^* \hat{c}(\omega) + G_c \hat{c}^\dagger(\omega)\right]\right.$$

APS Online Preprint

$$+\alpha_{\pm}\sqrt{\kappa_m}\hat{m}_{\rm in}(\omega)+\beta_{\pm}\,{\rm e}^{\theta_{\pm}}\sqrt{\gamma}\hat{b}_{\rm in}(\omega)\Big\}, \quad (7b)$$

where $\chi_j=[{\rm i}(\Delta_j-\omega)+\kappa_j/2]^{-1}$, $j=\pm,c$ are the susceptibilities of the supermodes and the cavity mode. As can be seen from the above equations, the phase factors of different input modes vary significantly in the dynamic response. As shown in Fig. 3(f), the phases of the susceptibilities of the hybridized supermodes are presented. Since the susceptibilities encode the system response, their phase structure plays a central role in signal transduction, enabling the manipulation of coherent interference via controlled mode hybridization.

3. Detection performance in CMM-based sensing

We consider the CMM as a detection device. The optical mode is employed as the output port due to its mature detection properties.[42] Both phonons and magnons can serve as probes for signal detection, enabling the sensing of mechanical or magnetic signals.[43] By analyzing the input spectrum of the optical mode, one can assess the system's signal detection performance. In general, signals are introduced via the input ports and couple to different modes depending on their nature.[44] For instance, magnonic signals enter through the m mode, whereas mechanical signals, such as mass, force, and displacement, are introduced through the b mode. These different input characteristics are also critical control factors when considering coherent noise cancellation or coherent signal amplification. Here, we focus solely on detecting quantum fluctuations in the system. Through conventional homodyne detection,[45] the system's output operator can be expressed as

$$\hat{M}_{\rm out}=\sum_{j=c,m,b}C_j(\omega)\hat{j}_{\rm in}+{\rm h.c.}, \quad (8)$$

where $C_j(\omega)$ denotes a dimensionless coefficient. For quantum systems, driving, noise, and signals can all be treated as system inputs in a unified manner. When the signal to be measured is sufficiently weak and much smaller than the driving strength, it can be regarded as a perturbation to the driving field during linearization and incorporated into the quantum noise operator.[46] Accordingly, the input operator becomes $\hat{k}_{\rm in}\to\hat{s}_{\rm in}+\hat{k}_{\rm in}$ $(k=b,m)$. The signal-independent part of the output operator constitutes the noise. To facilitate later comparison between different protocols, we define the added noise relative to the input signal

$$\hat{M}^k_{\rm add}(\omega)=\sum_{j=c,m,b}\frac{C_j(\omega)}{C_k(\omega)}\hat{j}_{\rm in}+{\rm h.c.}, \quad (9)$$

This definition of the relative added noise directly reflects the system's signal-to-noise ratio (SNR). The corresponding amplification parameter is given by

$$\hat{M}^k_{\rm ap}(\omega)=C_k(\omega)+C^*_k(\omega). \quad (10)$$

Here, we treat the signal under test as a real observable satisfying $\hat{s}^\dagger_{\rm in}=\hat{s}_{\rm in}$ and $\langle\hat{s}^\dagger_{\rm in}\hat{s}_{\rm in}\rangle=s$.[35,47,48] According to the standard spectral definitions, we obtain the system's SNR and gain spectra for a unit input signal as follows:

$$\begin{aligned}S^k_{\rm SNR}(\omega)&=\frac{1}{2}\left[\sum_{j=c,m,b}\left|\frac{C_j(\omega)}{C_k(\omega)+C^*_k(\omega)}\right|(2j_{th}+1)\right]^{-1},\\ S^k_{\rm ap}(\omega)&=|C_k(\omega)+C^*_k(\omega)|^2\\&=\left|\frac{\sum_{j=\pm}\sqrt{\kappa}(G_c\chi_c+{\rm c.c.})(\tilde{k}_j\mu_j\chi_j+{\rm c.c.})}{1+\sum_{j=\pm}|G_c\mu_j|^2(\chi_c-\chi^*_c)(\chi_j-\chi^*_j)}\right|^2,\end{aligned} \quad (11)$$

where we define $\tilde{m}_{\pm}=\alpha_{\pm}$ and $\tilde{b}_{\pm}=\beta_{\pm}{\rm e}^{\theta_{\pm}}$. According to the analysis in Fig. 1, our signal detection relies primarily on the quantum coherence between signals in supermodes, which allows for coherent signal amplification. Thus, the detection efficiency depends on the quantum coherence between the two supermode coefficients $(\tilde{k}_+\mu_+\chi_++\tilde{k}_-\mu_-\chi_-+{\rm c.c.})$ in $S^k_{\rm ap}(\omega)$. According to Fig. 3, we can obtain the argument information of the quantum coherence parameters $\tilde{k}_j\mu_j\chi_j$ in the vicinity of the EP, as shown in Table 1.

Table 1. The argument information of the quantum coherence parameters $\tilde{k}_j\mu_j\chi_j$ in the vicinity of the EP.

	G_p-0	G_p+0
${\rm Arg}(\tilde{m}_+\mu_+\chi_+)$	$\pi/2$	$-\pi$
${\rm Arg}(\tilde{m}_-\mu_-\chi_-)$	$-\pi/2$	0
${\rm Arg}(\tilde{b}_+\mu_+\chi_+)$	0	$\pi/2$
${\rm Arg}(\tilde{b}_-\mu_-\chi_-)$	π	$-\pi/2$

The detection performance of the system is strongly dependent on both the probing port and the phase relation between the hybridized supermodes, which is governed by the alternating influence of the $\mathcal{PT}$-symmetric and symmetry-broken regimes. For the $\hat{m}$ mode as the probing port, the phase behavior indicates that when $G_m<G_p$, the coherence parameters of the two supermodes exhibit a $\mathcal{PT}$-symmetric relation. In this regime, the amplification is enhanced as the system approaches the EP, implying that a stronger response can be achieved near criticality. In contrast, when $G_m>G_p$, the system enters the $\mathcal{PT}$-symmetry-broken regime, where the coherence between the supermodes favors amplification away from the EP. However, in this regime, the parameters μ_j decrease rapidly with increasing G_m (shown in Fig. 3), which suppresses the overall response. As a result, the detection performance for the $\hat{m}$ port exhibits nonmonotonic behavior. It first increases with G_m, then drops sharply near the EP, followed by a recovery beyond the EP, and finally decreases again at large G_m due to the suppression of μ_j.

For the $\hat{b}$ mode as the probing port, an opposite trend is observed. When $G_m<G_p$, the system resides in the $\mathcal{PT}$-symmetry-broken regime, where the amplification improves as the system moves away from the EP. Nevertheless, for very

CPB Online In Press

small G_m, the two modes become effectively decoupled, leading to the disappearance of well-defined supermodes and thus poor detection performance. When $G_m > G_p$, the system transitions to the $\mathcal{PT}$-symmetric regime, where the amplification is enhanced as the EP is approached. Consequently, the detection performance for the $\hat{b}$ port initially decreases with increasing G_m, then rises sharply near the EP, reaches a maximum at the EP, and finally decreases again in the strong-coupling regime. Overall, these results highlight that the optimal detection condition is highly sensitive to both the probing channel and the underlying $\mathcal{PT}$ phase, and that the EP plays a qualitatively different role depending on the measurement configuration.

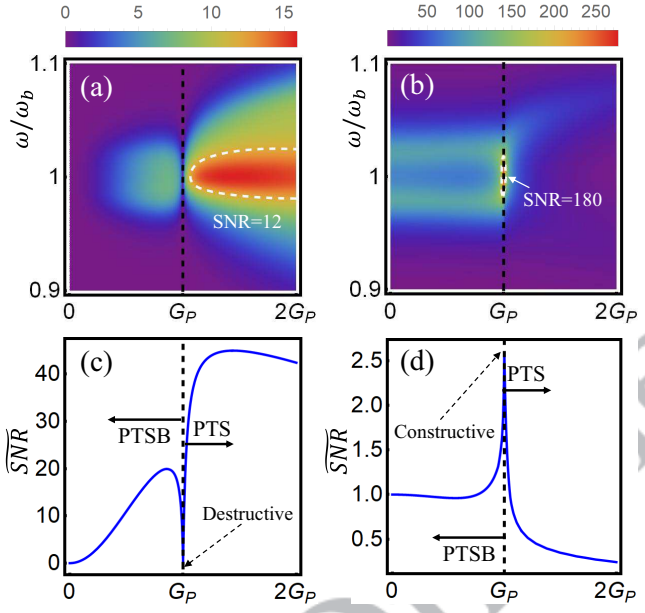


Fig. 4. SNR spectrum as a function of G_m for m-port detection (a) and b-port detection (b). (c) Ratio of the maximum SNR to that at strong coupling $G_m = \omega_b$ as a function of G_m for m-port detection. (d) Ratio of the maximum SNR to that without the m mode ($G_m = 0$) as a function of G_m for b-port detection. Other parameters are the same as in Fig. 2.

A more detailed numerical characterization of the CMM detection scheme is shown in Fig. 4. The density plots in Figs. 4(a) and 4(b), together with the corresponding maximum SNR curves in Figs. 4(c) and 4(d), illustrate the dependence of the detection performance on the coupling strength G_m for both m-port and b-port configurations. To better illustrate the performance enhancement of our scheme, Figs. 4(c) and 4(d) present the relative SNR, denoted as $\widetilde{\text{SNR}}$. In Fig. 4(c), for probing at the m port in the cascaded configuration, the intuitive trend is that stronger coupling leads to a higher SNR.[35] Here, the strong-coupling regime is taken as a reference, with the maximum SNR at $G_m = \omega_b$ used for normalization. In Fig. 4(d), for probing at the b port, the results are compared with the case without magnon coupling, using the maximum SNR at $G_m = 0$ for normalization. From the perspective of the original framework shown in Fig. 1(a), the CMM, whether operated in an indirect detection scheme (with $\hat{m}$ as the probing port and the output via $\hat{b}$) or a direct detection scheme (with $\hat{b}$ as the probing port assisted by the $\hat{m}$ mode), would intuitively suggest that increasing G_m always improves the detection performance.[34,35] However, the numerical results in Fig. 4 clearly demonstrate that this intuition is incomplete. We note that the dynamics in the supermode representation constitute a deformation of the original Hamiltonian dynamics, leaving the physical dynamical content unchanged. While the EP remains degenerate and inaccessible within the supermode formulation, its spectral properties can be recovered either through analytic continuation or by direct recourse to the original representation.

As analyzed above, under the alternating influence of the $\mathcal{PT}$-symmetric and symmetry-broken regimes, the system exhibits fundamentally different coherence behaviors depending on the detection port. For the chosen parameters, the local phase satisfies $\theta_\pm = -\pi/2$ at the EP, naturally leading to constructive interference for inputs from one channel and destructive interference for inputs from the other. For the m-port detection, destructive coherence emerges near the EP, leading to a suppression of the SNR in its vicinity, while the optimal detection performance appears in the regime $G_m > G_p$. In contrast, for the b-port detection, constructive coherence occurs near the EP, resulting in a pronounced enhancement of the SNR and an optimal detection performance around this point. This striking contrast provides a clear and physically transparent perspective for understanding the role of quantum coherence in the detection process. Notably, such coherence-induced interference effects are difficult to identify within the original framework, but become evident when analyzed in the supermode framework, where the interplay between hybridization and phase evolution can be explicitly resolved.

4. Discussion and conclusion

This work investigates the detection performance of a CMM-based sensing scheme from the perspective of mode hybridization and $\mathcal{PT}$-phase evolution. The supermode representation reveals that the detection characteristics are governed by the alternating influence of the $\mathcal{PT}$-symmetric and symmetry-broken regimes. Distinct interference behaviors emerge under different probing configurations. The numerical results show that the optimal SNR reaches max SNR ≈ 15 for the m-port and max SNR ≈ 250 for the b-port under the chosen parameters. This difference arises from the lack of optimization of the coupling parameter G_c, which controls the trade-off between backaction noise and shot noise. Such optimization has been extensively studied in conventional quantum coherent detection schemes,[35,36,49] but is not included here. Nevertheless, the relative variation of the SNR as a function of G_m clearly highlights the fundamental role of quantum coherence in shaping the detection performance. The enhancement originates from the $\mathcal{PT}$-symmetric to symmetry-broken

transition. Neither gain-loss balance nor strict phase-matching conditions are required. As a result, the scheme exhibits robustness against parameter fluctuations and driving perturbations. Within the supermode framework, the optimal detection regime can be directly identified through symmetry considerations. Notably, the EP does not universally maximize the detection performance; instead, the optimal regime depends on the probing port and the associated interference mechanism. This behavior is consistent with recent studies on EP-based sensing.[26,50–52]

The parameters considered in this work lie within experimentally accessible regimes in CMM and related hybrid platforms,[47,53,54] demonstrating feasibility with current technology. We establish a symmetry-based framework for quantum-coherent detection in hybrid systems. By exploiting mode hybridization, $\mathcal{PT}$-phase structure, and interference effects, we identify parameter regimes that enable enhanced detection performance. The analysis provides a route to optimal operation without relying on fine tuning around EPs.

Acknowledgments

Project supported by the Ningbo Natural Science Foundation (Grant No. 2025J137), the National Natural Science Foundation of China (Grant No. 12074206), and the Research Foundation of National Key Laboratory of Shock Wave and Detonation Physics (Grant No. 2024CXPTGFJJ06407).

References

[1] Clerk A A, Devoret M H, Girvin S M, Marquardt F and Schoelkopf R J 2010 *Rev. Mod. Phys.* **82** 1155
[2] Hou J, Zhu J, Ma R, Xue B, Zhu Y, Lin J, Jiang X, Zheng Y, Chen X, Cheng Y, Ge L and Wan W 2024 *Phys. Rev. Lett.* **132** 256902
[3] Xiao Z, Li H, Kottos T and Alù A 2019 *Phys. Rev. Lett.* **123** 213901
[4] Huai S N, Liu Y L, Zhang J, Yang L and Liu Y X 2019 *Phys. Rev. A* **99** 043803
[5] Hatano N and Nelson D R 1996 *Phys. Rev. Lett.* **77** 570
[6] Bender C M and Boettcher S 1998 *Phys. Rev. Lett.* **80** 5243
[7] Minganti F, Miranowicz A, Chhajlany R W and Nori F 2019 *Phys. Rev. A* **100** 062131
[8] Zhang Z, Wang Y P and Wang X 2020 *Phys. Rev. A* **102** 023512
[9] Saffman M, Walker T G and Mølmer K 2010 *Rev. Mod. Phys.* **82** 2313
[10] Graham T M, Song Y, Scott J, Poole C, Phuttitarn L, Jooya K, Eichler P, Jiang X, Marra A, Grinkemeyer B, Kwon M, Ebert M, Cherek J, Lichtman M T, Gillette M, Gilbert J, Bowman D, Ballance T, Campbell C, Dahl E D, Crawford O, Blunt N S, Rogers B, Noel T and Saffman M 2022 *Nature* **604** 457
[11] Barry J F, Schloss J M, Bauch E, Turner M J, Hart C A, Pham L M and Walsworth R L 2020 *Rev. Mod. Phys.* **92** 015004
[12] Bittner S, Dietz B, Günther U, Harney H L, Miski-Oglu M, Richter A and Schäfer F 2012 *Phys. Rev. Lett.* **108** 024101
[13] Quijandría F, Naether U, Özdemir S K, Nori F and Zueco D 2018 *Phys. Rev. A* **97** 053846
[14] Chen W, Zhang J, Peng B, Özdemir S K, Fan X and Yang L 2018 *Photon. Res.* **6** A23
[15] Zhang F, Feng Y, Chen X, Ge L and Wan W 2020 *Phys. Rev. Lett.* **124** 053901
[16] Peng P, Cao W, Shen C, Qu W, Wen J, Jiang L and Xiao Y 2016 *Nat. Phys.* **12** 1139
[17] Fan H, Chen J, Zhao Z, Wen J and Huang Y P 2020 *ACS Photonics* **7** 3035
[18] Alexeyev C N, Barshak E V, Lapin B P and Yavorsky M A 2023 *Phys. Rev. A* **107** 023522
[19] Ge L and Türeci H E 2013 *Phys. Rev. A* **88** 053810
[20] Wang J, Mukhopadhyay D and Agarwal G S 2022 *Phys. Rev. Res.* **4** 013131
[21] Feng L, El-Ganainy R and Ge L 2017 *Nat. Photon.* **11** 752
[22] Yang F, Liu Y C and You L 2017 *Phys. Rev. A* **96** 053845
[23] Nair J M P, Mukhopadhyay D and Agarwal G S 2021 *Phys. Rev. Lett.* **126** 180401
[24] Cao W, Lu X, Meng X, Sun J, Shen H and Xiao Y 2020 *Phys. Rev. Lett.* **124** 030401
[25] Kim J, Kim B and Kim S K 2025 *Phys. Rev. Lett.* **135** 116905
[26] Zhang T, He G C, Chen Z X, Zhang X, Lu M H and Chen Y F 2026 *Phys. Rev. B* **113** 104307
[27] Almanakly A, Assouly R, Kang H H, Gingras M, Niedzielski B M, Stickler H, Schwartz M E, Serniak K, Hays M, Grover J A and Oliver W D 2026 *Phys. Rev. Lett.* **136** 183601
[28] Vitanov N V 2021 *Phys. Rev. A* **103** 063104
[29] Peng Z H, Jia C X, Zhang Y Q, Yang Y and Kuang L M 2023 *Phys. Rev. A* **108** 033716
[30] Li B, Lu T X, Kuang L M, Jing H and Lee C 2025 *Phys. Rev. Appl.* **24** 044032
[31] Zuo X, Fan Z Y, Qian H, Ding M S, Tan H, Xiong H and Li J 2024 *New J. Phys.* **26** 031201
[32] Aspelmeyer M, Kippenberg T J and Marquardt F 2014 *Rev. Mod. Phys.* **86** 1391
[33] Jiang C, Song L N and Li Y 2018 *Phys. Rev. A* **97** 053812
[34] Wang X Y, Xiong B, Zhang W Z and Zhou L 2018 *Eur. Phys. J. D* **72** 117
[35] Zhang W Z, Chen L B, Cheng J and Jiang Y F 2019 *Phys. Rev. A* **99** 063811
[36] Xu D H, Liu Z and Yu C S 2025 *Phys. Rev. A* **111** 053508
[37] Liu Z, Liu Y, Yang Y and Yu C 2024 *Ann. Phys. (Berlin)* **536** 2400018
[38] Li W, Li C and Song H 2017 *Phys. Rev. A* **95** 023827
[39] Wang W C, Zhou Y L, Zhang H L, Zhang J, Zhang M C, Xie Y, Wu C W, Chen T, Ou B Q, Wu W, Jing H and Chen P X 2021 *Phys. Rev. A* **103** L020201
[40] Li B, Zhang Y, Wang J, Liu J, Li M, Wang W, Ma J, Yuan P, Zhang D, Zhu H, Zhang H and Qian L 2025 *Phys. Rev. Res.* **7** 023012
[41] Barral D, Walschaers M, Bencheikh K, Parigi V, Levenson J A, Treps N and Belabas N 2020 *Phys. Rev. A* **102** 043706
[42] Zhang C, Chen Y, Chen G, Sun H, Zhang J, Liu K, Yang R and Gao J 2024 *Phys. Rev. Appl.* **22** 054068
[43] Shen Z, Xu G T, Zhang M, Zhang Y L, Wang Y, Chai C Z, Zou C L, Guo G C and Dong C H 2022 *Phys. Rev. Lett.* **129** 243601
[44] Greco A, Fasolo L, Meda A, Callegaro L and Enrico E 2021 *Phys. Rev. B* **104** 184517
[45] Chen X, Xu F, Xu H and Zhang L 2022 *Phys. Rev. A* **106** L051702
[46] Li Z, Ren Z, Li Y, Liu Y C and Peng K 2019 *Phys. Rev. Appl.* **11** 064048
[47] Liu Z, Liu Y Q, Mai Z Y, Yang Y J, Zhou N N and Yu C S 2024 *Phys. Rev. A* **109** 023709
[48] Ghosh S, Carney D, Shawhan P and Taylor J M 2020 *Phys. Rev. A* **102** 023525
[49] Degen C L, Reinhard F and Cappellaro P 2017 *Rev. Mod. Phys.* **89** 035002
[50] Khanbekyan M 2023 *Phys. Rev. A* **108** 023710
[51] Zheng X and Chong Y D 2025 *Phys. Rev. Lett.* **134** 133801
[52] Jin Y, Li W, Djafari-Rouhani B, Torrent D, Xiang Y and Xuan F Z 2024 *Phys. Rev. Appl.* **22** 034026
[53] Jia J, Li Y, Huang J and Zhang M 2026 *Phys. Rev. A* **113** 013719
[54] Chen L, Liu Y, Bin L, Ye S Y and Zhong Z R 2025 *Phys. Rev. Res.* **7** 033157

Chinese Physics B Online First